Molecular Imaging of Shear-Induced Polymer Migration in Dilute Solutions near a Surface

Lin Fang,† Chih-Chen Hsieh,‡ and Ronald G. Larson*

Department of Chemical Engineering, University of Michigan, Ann Arbor, Michigan 48109

Received November 16, 2006; Revised Manuscript Received August 15, 2007

ABSTRACT: We measure the time-dependent concentration and stretch of λ-phage DNA molecules near a glass surface in torsional shear flow using epi-fluorescence microscopy. We find that the thickness of the depletion layer increases with increasing Weissenberg number over a time scale on the order of the time for diffusion across the depletion layer, in qualitative agreement with recent theory of Ma and Graham (2005) based on a FENE-P dumbbell model. However, the steady-state experimental depletion layer at high Weissenberg number ($Wi = 10$) is an order of magnitude thinner than expected from these predictions. The discrepancy is reduced to a factor of 2 in Brownian dynamics simulations of 10-spring chains. The remaining discrepancy suggests that more refined models of the migration phenomenon are required to obtain quantitative predictions. Over the time scale of migration, the apparent mean fractional stretch of DNA near the surface decreases with time, which we show could be caused by a few broken DNA fragments that are left near the surface when intact DNA diffuses away.

Introduction

Much work has been devoted over the years to understanding the dynamics and transport of polymer solutions near surfaces or in confined geometries because of the importance of this topic to colloid stabilization, surface protection, lubrication, chromatography, enhanced oil recovery, and the recently emerging microfluidic and nanofluidic techniques. The presence of a solid−liquid interface strongly affects the behavior of long polymer molecules in shear flow, inducing migration away from the surface for example.[1−5] Efforts to explain this phenomenon prior to 1994 were extensively summarized by Agarwal and co-workers.[6] Garner and Nissan[7] speculated that the spatial free-energy gradient could drive cross-streamline migration of a polymer molecule. However, Aubert and co-workers[8,9] pointed out that it is not clear that in a dilute polymer solution a spatial gradient in intramolecular free energy can result in a displacement of the center of mass of a polymer molecule. In some kinetic theories, a contribution to the polymer flux is predicted to arise from the divergence of the stress,[10] but in dilute solution this would lead to migration only in a nonhomogeneous flow gradient.[11]

The existence of a shallow depletion layer near a surface under no-flow conditions arises from the restricting influence of the surface on the conformational freedom of the polymer, which reduces its entropy, and induces it to migrate away from the surface. Such surface-induced depletion due to conformational entropy is predicted to occur over a distance comparable to the polymer's radius of gyration and to be either insensitive to the shear rate[12−16] or to decrease with increased shear rate,[17] in contrast to experiments[2,4,5] that show an increase in depletion layer thickness with increased shear rate.

Recently, Jendrejack and co-workers[18,19] performed Brownian dynamics (BD) simulations of dilute solution of flexible polymer molecules in flow through a microchannel with a square cross-section, accounting for intrachain hydrodynamic interactions (HI) and perturbations of HI due to the confining walls. The simulations predict that the molecules tend to migrate toward the centerline, forming wall depletion layers that are much thicker than the radius of gyration of the molecules. This prediction is consistent with recent experiments[4,5] of dilute DNA solutions undergoing pressure-driven flow in microchannels. Accounting for full HI in BD simulations, Chen et al. found that the thickness of the depletion layer for the DNA molecules near the surface in an oscillatory pressure-driven flow increases with increasing Wi,[5] in agreement with the experimental results.[4] However, their simulations also showed that the chain stretch near the surface increases with increasing Wi, which seems to conflict with recent experimental results.[4,20]

While the work of Jendrejack et al. and Chen et al. involved numerically intensive finite element and BD computation, a much simpler approach was recently developed by Ma and Graham[21] to describe the behavior of flowing polymer solutions near a single solid surface using a bead−spring dumbbell model for the polymer molecules, in which HI between the chains and the surface leads to migration away from the surface in shear flow. The model predicts that the chain density profile reaches steady state over a long time scale L_d^2/D, where D is the DNA center-of-mass diffusivity and where L_d is the thickness of the wall depletion layer.

Although these recent theoretical predictions explain qualitatively the observed depletion behavior, including the increased depletion layer thickness with increased shear rate, quantitative agreement has not yet been demonstrated. Here, we therefore measure experimentally the time-dependent stretch and concentration of λ-phage DNA molecules in a torsional shear flow using epi-fluorescence microscopy. In microchannels, due to the very slow approach to steady state and the finite residence time of the polymer molecules, a fully developed concentration profile in steady flow is difficult to attain. However, in a torsional shear flow, DNA molecules can remain in the flow cell for an indefinite amount of time as they are stretched and migrate away from the surface, which allows realization of a fully developed concentration profile in steady flow. To compare

* Corresponding author. E-mail: rlarson@umich.edu.
† Current address: DuPont China Research and Development Center, Zhangjiang Hi-Tech Park, Shanghai, 201203, People's Republic of China.
‡ Current address: Dept. of Chemical Engineering, Massachusetts Institute of Technology, Cambridge, MA 02139.

10.1021/ma062630c CCC: $37.00
Published on Web 10/11/2007

Table 1. Sizes of λ-Phage DNA-Hind III Digest Fragments

fragment	size(bp)	fragment/full chain
1	23 130	0.48
2	9416	0.19
3	6557	0.14
4	4361	0.09
5	2322	0.05
6	2027	0.04
7	564	0.01
8	125	0.00

with the experimental results, we also perform BD simulations of bead−spring chains, with multiple springs and full HI, using an HI tensor that includes the wall effect.

Experimental Section

Experimental Setup. The torsional flow cell was mounted on the motorized stage of a Nikon TE200 fluorescence microscope, with the upper plate rotated by a motor, while the lower plate was a replaceable glass coverslip.[20,22] The alignment method was described by Li et al.,[20] and detailed particle image velocimetry (PIV) measurements of the flow field were performed,[22] and these confirmed that the expected simple shearing flow was generated by the flow cell.

Preparation of Intact λ-Phage DNA Solution. In our work, the concentration of fluorescently labeled λ-phage DNA in the final solutions was around 60∼65 pg/μL, which is in the very dilute regime, about 3 orders of magnitude below the overlap concentration of the DNA molecules. The λ-phage DNA solutions were prepared using the following protocol. A stock solution of 48.5-kbp λ-phage DNA molecules (New England BioLabs) at a concentration of 0.5 mg/mL was diluted 40-fold in TE10 buffer (10 mM Tris-HCl, 1 mM EDTA, 10 mM NaCl, pH 8.0) and heated to 65 °C for 10 min to free the DNA's complementary sticky ends, and then quickly cooled to room temperature. A stock solution of YOYO-1 dye (Molecular Probes) at a concentration of 1 mM was diluted 100-fold in the TE10 buffer. Then the diluted YOYO-1 solution was mixed with the diluted DNA solution at a volume ratio of 1:5 and incubated for a minimum of 2.5 h at room temperature in the dark. As a result, the λ-phage DNA was fluorescently labeled with YOYO-1 at a dye:base pair molar ratio of about 1:10. While unstained λ-phage DNA has a contour length $L = 16.3\ \mu$m,[23] for a λ-phage DNA molecule labeled with YOYO-1 at a dye:base pair molar ratio of 1:4, $L \approx 22\ \mu$m.[24−26] Assuming that the length of a DNA molecule increases linearly with the ratio of dye:base pair, we estimate $L \approx 19.0\ \mu$m for our stained λ-phage DNA. We made sucrose solutions of various concentrations by dissolving sucrose (Crystalline/Certified ACS, Fisher Chemical) into a pH 8.0 TE buffer consisting of 10 mM Tris-HCl, 2 mM EDTA, and 10 mM NaCl. β-mercaptoethanol is an antioxidant, and the sucrose solution was used as a viscosifier. Then the labeled λ-phage DNA solution was mixed with β-mercaptoethanol (Sigma) and the sucrose solution at a volume ratio of 1:6:143. To avoid the breakage of DNA chains, after mixing the sucrose solution and β-mercaptoethanol with a vortex mixer, we added the stained DNA solution into the above solution with a large-orifice pipet tip (Fisher), rotated the glass vial very gently by hand for about 2 min, and then left the solution in a dark drawer at room temperature for about 16 h. The final EDTA concentration in the solution is close to 2 mM EDTA, because the volume of stained DNA solution (which had 1 mM EDTA) is small.

Preparation of Mixture of Intact λ-Phage DNA and Its Hind III Digest. Intact λ-phage DNA was mixed with a λ-phage DNA Hind III digest (New England Biolabs) at mass ratios of 91:9, and 70:30. The Hind III digest of λ-phage DNA yields eight fragments (see Table 1). However, due to the resolution of the microscopic image, mainly only the two largest fragments can be visualized and recognized as DNA through the microscope. (The others are either invisible or appear as small dots that are ignored as possible impurities.) The same procedure as used for the intact DNA was applied to fluorescently label the λ-phage DNA Hind III digest with YOYO-1 at a dye:base pair molar ratio of about 1:10. The mixture of DNA molecules was diluted in the same way as above. We also diluted only a λ-phage DNA Hind III digest in a solvent. The concentrations of DNA in all these solutions were around 60∼65 pg/μL.

Determination of Shear Rate and DNA Relaxation Time. The Weissenberg number ($Wi = \dot{\gamma}\tau$, with $\dot{\gamma}$ the applied shear rate, and τ the polymer's longest relaxation time) is used to characterize the flow strength. In our torsional shear cell, with a gap size of $h_{gap} = 0.5$ mm and a top-plate rotational speed $\omega = 6.36 \times 10^{-2}$ rev/s, the shear rate at $r = 3.0$ mm from the rotation axis is

$$\dot{\gamma} = \frac{2\pi\omega r}{h_{gap}} = 2.4\ \text{sec}^{-1} \tag{1}$$

Theoretically, the relaxation time of a DNA molecule is linearly proportional to the solvent viscosity η_s.[27] Using data collected mostly from papers of Chu and co-workers, a linear relationship between τ and η_s has been constructed for λ-phage DNA, namely[4]

$$\tau\ (\text{s}) = 0.094\ \eta_s\ (\text{cP}) \tag{2}$$

Using solutions of three different solvent viscosities: $\eta_s = 22.1$, 46.0, and 90.2 cP (measured by TA Instrument AR1000 controlled stress rheometer), we obtain relaxation times of $\tau = 2.1$, 4.3, and 8.5 s, respectively, in these three solvents. For the prescribed shear rate of 2.4 s^{-1}, we calculate $Wi = 5.0$, 10.3, and 20.4, respectively.

Image Acquisition and Analysis. We visualized stained λ-phage DNA molecules using the Nikon TE200 fluorescence microscope with a 100 × 1.3 objective, and a digital interline CCD camera CoolSNAP HQ (Roper Scientific) to capture images at a resolution of 1392 × 1040 pixels using full-chip acquisition. The image acquisition software MetaVue/MetaMorph version 4.5 (Universal Image, distributed by Fryer Co.) was used to control the camera, the XYZ stage motor (Prior Inc.), and the electronic shutter (Uniblitz VMM-D1, Vincent Associates).

Using a micrometer, the top surface was brought into contact with the bottom surface to zero the gap on the micrometer reading. In the horizontal plane, the center of the top plate, which corresponds to the axis of rotation, was taken as the origin of our coordinate system. A 0.3 μL droplet of an extremely dilute fluorescent silica particle (0.8 μm in diameter) aqueous dispersion was dispensed onto the bottom coverglass at (0, 3000 μm), so that less than 8 particles appeared in an image frame of 92 × 69 μm. Since the particle density of ∼2.0 g/mL is higher than the DNA solution density of 1.2−1.3 g/mL, those particles settled to the bottom surface and served as markers to locate the bottom surface in the microscope. After the dispersion of particles dried out, a 600 μL DNA solution was loaded into the shear cell using a large-orifice pipet tip (Fisher) to minimize the chances of breaking the DNA molecules, and the top plate was lowered to 500 μm above the bottom surface using the micrometer. To block the evaporation of the solution, a volume of 100 μL silicone oil (Fisher Chemical) was added to seal the gap between the top plate and the side-wall of the cell. The solution then relaxed for half an hour.

In the static solution, to obtain the density of DNA molecules in the bulk solution, 200 images with 40 ms exposure time were taken at different positions distributed in the solution at a distance of at least 35 μm above the bottom surface, which allows the average number of DNA molecules per frame to be determined to within 2.5%.

In the torsional shear flow, to calculate statistically accurate values of concentration and polymer stretch at each time point for a specific distance above the bottom surface, we obtained images over a long enough time interval to allow a sufficient number of molecules to move into the image window. We also wished to keep the time interval as short as possible, so that the data averaged over the interval might represent reasonably well a single-time point. On the basis of our experience, at least 100 images (each containing multiple DNA molecules) are needed for each time interval and

Table 2. Flow Velocity and Time Interval to Acquire 100 Images at 1−10 μm Above the Bottom Surface

H (μm)	1	3	5	7	10
v_f (μm/s)	2.4	7.2	12.0	16.8	24
t_i (min)	19.8	6.6	6.6	5.0	3.3

vertical position. The time interval required for new molecules to move into each image is determined by the flow velocity at a given vertical position. At the distances $H = 1-10$ μm above the surface, the flow velocity v_f, and the time interval t_i required to acquire 100 images are all given in Table 2.

At $H = 1$ μm, the flow velocity is very low, which results in a 19.8-min total time interval needed to obtain 100 images. This is too crude to demonstrate the time dependence of concentration and polymer stretch. In addition, because of the migration away from the surface, there are not enough DNA molecules at $H = 1$ μm in only 100 images to be able to measure accurately the mean polymer stretch. Therefore, in this paper, we only consider the measurements for $H = 3-10$ μm.

The stage was moved to the reference horizontal position, which we designate (0, 3000 μm), and the marker particles were imaged to determine the vertical location of the bottom surface. Then the objective was raised to the desired vertical focal position. Rotation of the top plate began at time zero. 100 images were taken in each time interval. To avoid artificially elongating the molecules due to image blurring under flow, the exposure time was limited to 40 ms at $H = 3$ μm and then decreased gradually to 20 ms for $H = 10$ μm, which is much smaller than the time for DNA molecules to diffuse out of the 1 μm depth of focus.

The offline software MetaVue version 4.6r1 (Universal Imaging Corporation) was used to analyze the images. In our analysis, we included only molecules that were sharply focused, estimated from the experiments to be within ± 0.5 μm of the focal plane. The number of DNA molecules in each image was manually counted. The number density of DNA molecules at each vertical position for each time period during the shear flow was normalized by the DNA number density in the static solution. We used the contour length of labeled λ-phage DNA, namely, $L = 19$ μm, to normalize the mean stretch of DNA molecules averaged over more than 300 molecules for each data point.

Simulation Method. As mentioned earlier, the phenomenon of shear-induced polymer migration has been modeled both in a channel[18,19] and in a slit[5,28,29] by BD simulations with the bead−spring model including full HI, where a finite element method was used to obtain the hydrodynamic tensor with the wall effect included. While this method is successful, the hydrodynamic tensor must be recomputed numerically for different channel geometries. Here, we used a simple formula for describing the HI between two spheres near a single flat solid boundary that can be easily applied in BD simulations. We followed the simulation technique described by Hsieh et al.[30] with a modified Rotne−Prager−Yamakawa (MRPY) tensor to describe the HI between beads in a bead−spring polymer chain with the presence of a nearby flat stationary boundary. We only briefly describe the method of BD simulations here and leave the details for readers to find in the reference.

The force balance equation on the ith bead with HI can be described as

$$\frac{d\mathbf{r}_i}{dt} = \kappa\cdot\mathbf{r}_i + \sum_{j=1}^{N}\frac{\partial}{\partial\mathbf{r}_j}\cdot\mathbf{D}_{ij}^T + \sum_{j=1}^{N}\mathbf{D}_{ij}\cdot\mathbf{F}_j^b + \left(\frac{6}{\Delta t}\right)^{1/2}\sum_{j=1}^{i}\boldsymbol{\sigma}_{ij}\cdot\mathbf{n}_j \quad (3)$$

where $\kappa = \nabla\mathbf{v}^T$ is the transpose of the velocity gradient tensor, N is the number of beads, $\mathbf{n}_j$ is a random vector uniformly distributed in each of three directions over the interval [-1,1], $\mathbf{r}_i$ is the coordinate vector of bead i, and $\mathbf{F}_j^b$ is the total of the spring and excluded volume forces acting on bead j. For interior beads the total spring force $\mathbf{F}_j^{sp,b}$ is

$$\mathbf{F}_j^{sp,b} = \mathbf{F}_j^{sp} - \mathbf{F}_{j-1}^{sp} \quad (4)$$

where $\mathbf{F}_j^{sp}$ is the force that spring j exerts on bead j. For the end beads,

$$\mathbf{F}_1^{sp,b} = \mathbf{F}_1^{sp},\ \mathbf{F}_N^{sp,b} = -\mathbf{F}_N^{sp} \quad (5)$$

The diffusion tensor $\mathbf{D}_{ij}$ describes the effect of HI on bead i induced by a force acting on bead j. From the fluctuation−dissipation theorem, the weighting factor $\boldsymbol{\sigma}_{ij}$ in eq 3 must satisfy the condition

$$\mathbf{D}_{ij} = \sum_{l=1}^{N}\boldsymbol{\sigma}_{il}\cdot\boldsymbol{\sigma}_{jl}^T \quad (6)$$

For BD simulations in bulk solutions, HI is usually described by the Rotne−Prager−Yamakawa (RPY) tensor.[31,32] However, the RPY tensor does not include the wall HI effect which has been shown to be the cause of the shear-induced migration of polymers. Thus, to correctly simulate the DNA migration phenomenon, the wall HI effect must be either estimated numerically or represented analytically by an MRPY tensor. Fortunately, such a tensor for the case of a semiinfinite domain bounded by one flat wall has been developed by Bossis et al.[33] and can be rewritten as

$$\boldsymbol{\Omega}_{ij}^{MRPY} = \boldsymbol{\Omega}^{RPY}(\mathbf{r}_i,\mathbf{r}_j) - \boldsymbol{\Omega}^{RPY}(\mathbf{r}_i,\mathbf{r}_j') + \Delta\boldsymbol{\Omega}^{RPY,wall}(\mathbf{r}_i,\mathbf{r}_j') \text{ if } |\mathbf{r}_i - \mathbf{r}_j| \geq 2a \quad (7)$$

where $\mathbf{r}_j'$ is the image of $\mathbf{r}_j$ relative to the wall. The detailed expression of each term, as well as the relationship between the above HI tensor and the diffusion tensor $\mathbf{D}_{ij}$ can be found in the Appendix. This formula for the MRPY tensor is only positive definite when two beads are not overlapped and another formula is needed to describe the interactions when the beads overlap. We notice that the overlap of spheres is actually unphysical, and the RPY tensor for overlapping spheres is ad hoc. Therefore, little is lost if we use a different ad hoc form in case of overlapping spheres, in which the HI corresponds to spheres that are just touching, and not overlapping, namely

$$\boldsymbol{\Omega}_{ij}^{MRPY} = \boldsymbol{\Omega}^{RPY}(\bar{\mathbf{r}}_i,\bar{\mathbf{r}}_j) - \boldsymbol{\Omega}^{RPY}(\bar{\mathbf{r}}_i,\bar{\mathbf{r}}_j') + \Delta\boldsymbol{\Omega}^{RPY,wall}(\bar{\mathbf{r}}_i,\bar{\mathbf{r}}_j'), \quad \text{if } |\mathbf{r}_i - \mathbf{r}_j| < 2a$$

$$\bar{\mathbf{r}}_i = \frac{\mathbf{r}_i + \mathbf{r}_j}{2} + a\frac{\mathbf{r}_i - \mathbf{r}_j}{|\mathbf{r}_i - \mathbf{r}_j|}, \quad \bar{\mathbf{r}}_j = \frac{\mathbf{r}_i + \mathbf{r}_j}{2} - a\frac{\mathbf{r}_i - \mathbf{r}_j}{|\mathbf{r}_i - \mathbf{r}_j|} \quad (8)$$

To test the proposed MRPY tensor given by eqs 7 and 8, we carried out BD simulations with a bead−spring model using the above MRPY tensor in the bulk, and find that the resulting center of mass diffusion coefficient differs by less than 0.2% from that obtained using the usual Rotne−Prager tensor. The relaxation times obtained using the two methods are also nearly identical. Although this approach for overlapping spheres works well for simulating DNA in water with excluded volume effect, the diffusion tensor could still become non-positive-definite for some configurations when excluded volume force is turned off. Therefore, use of the MRPY tensor for overlapping spheres is not yet a universal solution.

We use a slightly smaller bead radius $a = 0.07$ μm instead of 0.077 μm used by Jendrejack et al.[34] since the former gives a longest relaxation time in better agreement with the measured one for λ-phage DNA. The intramolecular excluded volume potential is[34]

$$U_{ij}^{ev} = \frac{1}{2}\upsilon k_B T N_{k,s}^2\left(\frac{3}{4\pi S_s^2}\right)\exp\left[\frac{-3|\mathbf{r}_j - \mathbf{r}_i|}{4S_s^2}\right] \quad (9)$$

where $\mathbf{r}_i$ and $\mathbf{r}_j$ are the position vector of beads i and j; k_B is Boltzmann's constant; υ is the excluded volume parameter; $N_{k,s}$ is the number of Kuhn steps per spring; $S_s^2 = N_{k,s}b_k^2/6$ and b_k is the Kuhn step length. We note that a more detailed model of DNA by Harnau et al.[35] requires a much smaller bead radius (1.35 nm) to obtain good predictions of dynamic structure factor over a wide

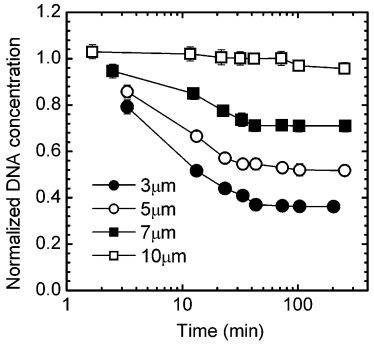

Figure 1. Normalized DNA concentration of λ-phage DNA molecules vs time at $H = 3-10$ μm above the bottom surface and $Wi = 10.3$. The error bars are standard errors.

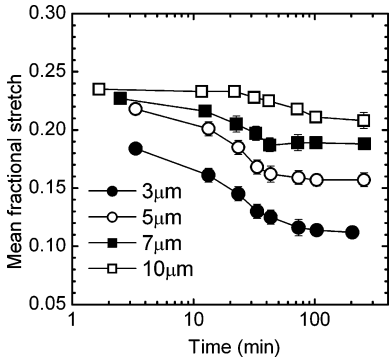

Figure 2. Same as in Figure 1, except for mean fractional stretch, rather than normalized DNA concentration.

Table 3. Parameters Used in the BD Simulation

L (μm)	no. of beads	a (μm)	$\tau_{1,\mathrm{sim}}$ (s)	b_k (μm)	ν (μm^3)	η_s (cP)
21.0	11	0.07	4.46	0.106	0.0012	46.0
10.5	6	0.07	1.49	0.106	0.0012	46.0
5.25	3	0.07	0.47	0.106	0.0012	46.0

range of wavenumbers. Here, however, our interest is only in the diffusion of the molecule as a whole, and for this purpose, coarse-grained models with few, and large, beads have been found to be adequate.[34]

In addition to the intramolecular excluded volume force, another excluded volume force is applied between the wall and the beads to prevent the beads from moving into the wall. This wall potential is[34]

$$U^{wall}(h) = -A_{wall} b_k^{-1} \delta_{wall}^{-2} (h - \delta_{wall})^3 \qquad (10)$$

where $A_{wall} = 25k_BT/3$ is the wall excluded volume parameter; and h is the shortest distance between the wall and the center of a bead; $\delta_{wall} = 0.236$ μm is the truncated distance of this potential. The wall potential is set to zero when $h > \delta_{wall}$. Since this wall excluded volume force is short-ranged, the thickness of the depletion layer is not affected. The parameters used in our BD simulation are summarized in Table 3.

Results and Discussion

Intact λ-Phage DNA at $Wi = 10.3$. To compare the concentration and polymer stretch profiles under different conditions, we plot in Figures 1 and 2 the average concentration and stretch against the center point of the time interval over which each set of 100 images was collected. Figures 1 and 2 show that at $Wi = 10.3$ with a solvent viscosity of 46.0 cP, after about 70 min, both normalized concentration and mean fractional stretch reach steady state. The formation of a depletion layer is driven by the migration of DNA molecules induced by HI between the surface and the molecular chain, as predicted

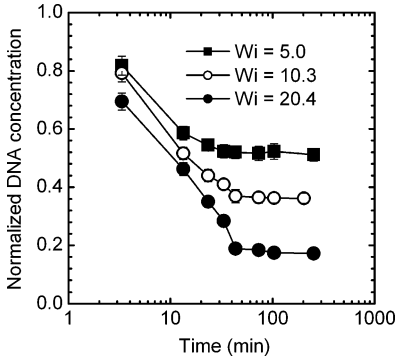

Figure 3. Normalized DNA concentration of λ-phage DNA molecules vs time at $H = 3$ μm and various Wi. The error bars are standard errors.

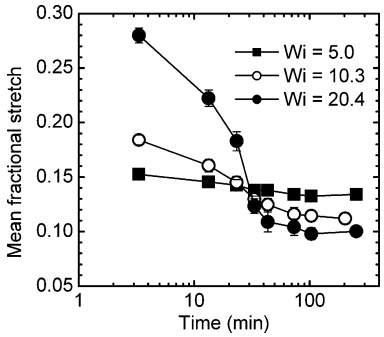

Figure 4. Same as in Figure 3, except for mean fractional stretch, rather than normalized DNA concentration.

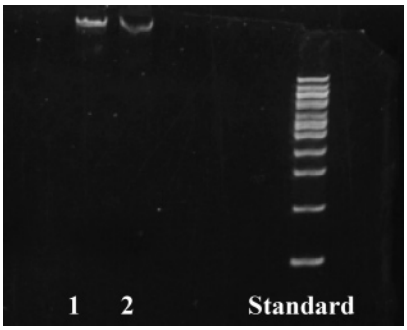

Figure 5. Gel-electrophoresis of DNA samples (10% polyacrylamide gel). Sample 1: stained λ-phage DNA in TE buffer, ~0.01 μg/μL. Sample 2: stained λ-phage DNA in a sucrose solution concentrated using a Microcon YM-30 (Millipore Co.). DNA standard ladder sequence: 100−1600 bps.

and observed in previous studies.[2,4,5,18,19,21] Under static, no-flow, conditions (at time zero), there is a thin depletion layer around 1 μm thick, owing to the finite radius of gyration of the DNA polymer, as mentioned in earlier work,[4] and not shown in Figure 1.

By using a bead−spring dumbbell model of the polymer above a single surface, Ma and Graham[21] predicted the temporal development of the concentration profile in uniform shear flow above a single wall at a variety of Weissenberg numbers, including $Wi = 10$. Applying their predictions with the stress relaxation time $\lambda_H = 4.3$ sec, and the length unit $\sqrt{k_BT/H_s} = \sqrt{2}R_g \approx 1\mu m$ (H_s is the dumbbell spring constant; T is the absolute temperature; R_g is the radius of gyration) corresponding to our DNA solution, we find from Figure 5 of Ma and Graham that the concentration profile is not even close to being at steady-state even at a time of 10 000 times λ_H, which is 12 h for our solution, for which $\lambda_H = 4.3$ s. This is much greater than the time of around 70 min that we observed. Moreover, the depletion layer thickness, measured by the distance from the wall at which

the concentration reaches 50% of the bulk value, is predicted to be around 50 times $\sqrt{k_BT/H_s}$ at steady state, which is around 50 μm, much greater than the value of 5 μm observed for our solution.

The measured diffusivity of λ-phage DNA in water at 24 °C is 0.47 $\mu m^2/s$.[36] Since the diffusivity is inversely proportional to the solvent viscosity, we estimate the DNA diffusivity as $D = 0.01$ $\mu m^2/s$ in our solvent of viscosity 46.0 cP, and therefore predict that the chain density profile should reach steady state over a time scale $L_d^2/D = 40$ min for the observed depletion layer thickness $L_d = 5$ μm, which is reasonably close to our experimental transition time of 70 min. Thus, the very long time predicted by Ma and Graham[21] for the concentration profile to reach a steady state is associated with the very thick depletion layer predicted, and if the thinner layer that we actually observe could be explained, then the time required to obtain this thinner boundary layer would be explained as well. While it was earlier suggested by Chen et al.[5] that the thinner depletion layer might be the result of polymer−polymer interactions, this cannot be the case for our very dilute samples, which show a deviation from theory similar to that shown for the more concentrated samples.[5]

The use of a dumbbell model is a likely contributor to the discrepancy between the theory of Ma and Graham and our experiments. In a shear flow, the FENE-P dumbbell is able to reach nearly 100% extension at high *Wi*, which is not observed in either experiments or in more sophisticated multiple-spring models, which only achieve around 50% extension at asymptotically high *Wi*.[26,34] This difference is significant, since the nearly complete extension possible for the dumbbell model means that the normal stresses, which diverge at full spring extension, are unlimited in magnitude for the dumbbell model. Since the normal stress, or spring tension, drives the polymer migration, this implies that for the dumbbell model, the depletion layer thickness should grow unboundedly thick for very high *Wi*. And, indeed, Figure 4 of Ma and Graham shows that the depletion layer thickness grows as the $^2/_3$ power of Wi at high *Wi*, the same power law with which the first normal stress difference grows with *Wi* for the FENE-P dumbbell model.[37] Thus, not surprisingly, the dumbbell model is too crude to give even qualitatively accurate predictions for the depletion layer thickness at high *Wi*.

In the torsional flow, due to the curvature of the streamlines, there is also a radial migration, whose rate can be estimated from the approximate expression,[38]

$$v_r^m = -\frac{\eta_s \dot{\gamma}^2(r)}{r k_B T} R_g^{\,5} \tag{11}$$

Substituting eq 1 into 11, we obtain

$$v_r^m = -\frac{4\pi^2 \omega^2 \eta_s R_g^{\,5}}{k_B T h_{gap}^{\,2}} r \tag{12}$$

In our experiments, with rotational rate $\omega = 6.36 \times 10^{-2}$ rev/s, solvent viscosity $\eta_s = 4.6 \times 10^{-2}$ Pa·s, radius of gyration $R_g = 7.6 \times 10^{-7}$ m, absolute room temperature $T = 298$ K, gap size $h_{gap} = 5.0 \times 10^{-4}$ m, $k_B = 1.381 \times 10^{-23}$ m^2 kg s^{-2} K^{-1}, the time for molecules to migrate radically from r_1 to r_2 can be calculated in seconds as

$$\Delta t = \int_{r_1}^{r_2} \frac{dr}{v_r^m} = 5.29 \times 10^5 (\ln r_1 - \ln r_2) \tag{13}$$

Thus, migration from $r_1 = 3.1 \times 10^{-3}$ m to $r_2 = 3.0 \times 10^{-3}$ m takes $\Delta t = 300$ min. This means that 300 min are required for molecules close to the imaging point ($r = 0.003$ m) to migrate 100 μm, which is the size of the imaging window and which is much smaller than the plate radius. Therefore, during the first 300 min of our experiments, the radial migration effect can be neglected.

Our experimental results are the first that allow an investigation of the conformation of molecules during their migration away from the bottom surface. Although the steady-state mean fractional stretch as a function of distance from the surface is consistent with our previous experimental results,[4,20] theoretical work[21] implies that the presence of the nearby surface should not affect the stretch of the molecule at a given *Wi*. Also, in start-up of shear flow, it only takes about 100 strain units for the average polymer stretch in the bulk to reach its plateau value.[39] Therefore, at a shear rate of 2.4 s^{-1}, after 1 min, the stretch should reach its steady state, whether or not migration is still occurring, because the DNA molecules are too dilute to affect each other's stretch. From Figure 2, however, it is obvious that the mean fractional stretch continues to change over a time scale much larger than needed for the stretch of a single molecule to reach its steady-state value, and in fact, it is the same time scale over which migration occurs.

***Wi* Dependence of DNA Migration.** To see how *Wi* affects the migraton and stretch, we also conducted experiments at *Wi* = 5.0 and 20.4 at $H = 3$ μm. The results given in Figure 3 show that the plateau value of the concentration decreases with increasing *Wi*, presumably because of the stronger HI between the surface and the polymer chain at higher *Wi*. The results indicate that the depletion layer thickness increases at increased *Wi*. With an increase of *Wi* from 5.0 to 20.4, the time for the stretch to reach its steady-state value increases from 40 min to 100 min. Remember that the chain density profile should reach steady state over a time scale L_d^2/D. In our experiments, the observed depletion layer thickness L_d increases with increasing *Wi*, and the increased *Wi* is created by increasing the viscosity of the solution, which leads to a decrease in the diffusivity *D*. Thus, L_d^2/D should increase with increasing *Wi*, in agreement with our experimental results.

Figure 4 indicates that for *Wi* ranging from 5.0 to 20.4, over the time scale of migration, the mean fractional stretch decreases with time and reaches a plateau value, which is probably due to the selective migration of longer chains away from the surface, as will be discussed below. At early time, the mean fractional stretch increases with increasing *Wi*, which agrees with the results in the bulk. However, after about 30 min, the mean fractional stretch decreases with increasing *Wi*, which is presumably related to the stronger HI between the surface and the polymer chain at higher *Wi*.

Molecular-Weight Dependence of DNA Migration. The above results imply that there is a coupling between the concentration and the stretch, because they both change over the same time scale. Given that the solution is dilute, and the molecules should migrate independently of each other, the only reasonable explanation seems to be that there are broken chains in the DNA sample, which remain near the surface as the unbroken chains selectively diffuse away, thus leading to a slow decrease in apparent mean fractional stretch near the surface. The degradation leading to broken chains might occur during the preparation and handling by the manufacturer or the user, and might be aggravated by the presence of low ionic strength of Na^+.[40] In principle, one could carry out gel electrophoresis to detect the fragments, but in practice ordinary gels do not

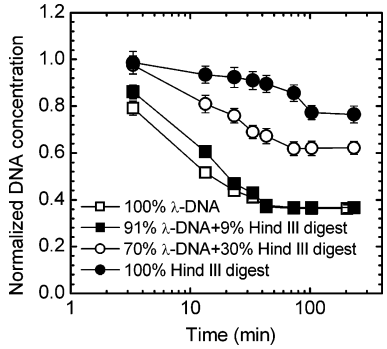

Figure 6. Normalized DNA concentration vs time of λ-phage DNA molecules, λ-phage DNA Hind III digest, and mixtures of them at $H = 3$ μm and $Wi = 10.3$. The error bars are standard errors.

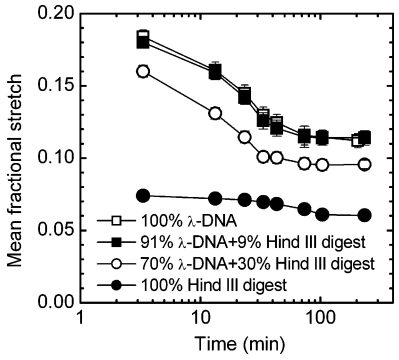

Figure 7. Same as in Figure 6, except for mean fractional stretch, rather than normalized DNA concentration.

provide enough sensitivity to detect molecules which have a wide range of lengths at low concentration. We performed gel-electrophoresis of DNA samples after staining with YOYO-1 and diluting with the sucrose solution in a 10% polyacrylamide gel (see Figure 5), which shows only a single band for each sample, corresponding to the original unbroken DNA chains.

Since our samples are in the very dilute regime, other techniques are not applicable to directly detect the broken chains. Thus, to investigate how the DNA fragments might affect the migration and stretch, we mixed nominally intact λ-phage DNA molecules with fragments deliberately introduced using a λ-phage DNA Hind III digest. Remember that primarily only the two largest fragments, which are around 50% and 20% of the length of the intact λ-phage DNA can be clearly distinguished as DNA molecules in the microscope. We performed the experiments at $H = 3$ μm with a solvent viscosity $\eta_s = 46.0$ cP and the prescribed shear rate of 2.4 s^{-1}, which corresponds to $Wi = 10.3$ for 19 μm long DNA molecules. For a given solvent viscosity, the relaxation time is proportional to the polymer contour length to a power of around 1.6,[40] therefore, the shorter chains possess a shorter relaxation time, which results in a smaller Wi for these molecules, and hence they should stretch less and migrate less.

Figures 6 and 7 point out that the normalized concentration and mean fractional stretch of the mixtures decrease over the same time scale, which again indicates the coupling between the concentration and the stretch. With an increase in the concentration of the shorter chains, the migration rate is weakened due to the weaker HI between the surface and the shorter chains, which agrees well with theoretical predictions,[18,19] and the mean fractional stretch (normalized by $L = 19$ μm) decreases due to the higher concentration of fragments. Surprisingly, the addition of 9% λ-phage DNA Hind III digest to a nominally pure λ-phage DNA solution does not produce a

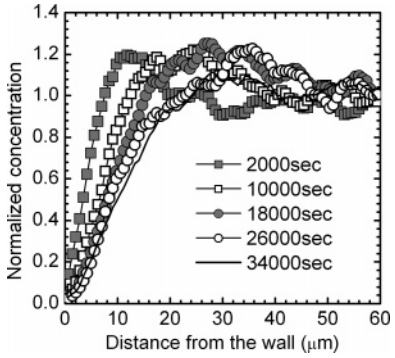

Figure 8. Normalized DNA concentration near an isolated surface as a function of time from BD simulations of 21 μm-long DNA at $Wi = 10$ using a bead−spring model with 11 beads.

significant change in the concentration or the stretch profiles, although during the first 30 min, the migration rate is lower in the mixed sample than in the intact one. When the concentration of the Hind III digest is increased to 30% of the total DNA mass, we observed a significant increase of the concentration and decrease of the stretch near the surface. For the sample containing only DNA Hind III digest, only about 20% of the chains migrate away from the surface region ($H = 3$ μm) at steady state, and the stretch also decreases slightly due to migration. The above results imply that the presence of DNA fragments decreases the stretch and increases the concentration near the surface, which could be the cause of the decrease of the mean fractional stretch in the intact DNA solution. Because the shorter chains migrate more weakly than the long chains, the flow selectively drives the longer chains away from the surface resulting in a lower mean fractional stretch near the surface.

Comparison of Experimental Results with BD Simulation Predictions. The dumbbell theory of Ma and Graham[21] shows that the time scale over which migration occurs is remarkably large; even after 10^4 relaxation times, the steady state of the concentration profile has not been reached at $Wi = 10$. In our experiments, however, steady state is attained after around 10^3 relaxation times for $Wi = 10$. In addition, the model[21] predicts an overshoot in concentration near the surface as a function of time, which we do not see in our measurements, possibly due to the average of data over a discrete time interval. (We note that a spatial overshoot was observed in an earlier study from our lab in the slit flow geometry, consistent qualitatively with theory.[4]) Moreover, the dumbbell theory also predicts a much thicker steady-state depletion layer of around 50 μm than we see in our experiments. As some of the discrepancies between our experimental results and the theory of Ma and Graham are likely due to their use of an oversimplified dumbbell model, we performed bead−spring BD simulations (see Table 3 for the parameters used in the simulation) of DNA molecules in shear flow near a single surface by using an MRPY tensor (see the Appendix for the derivation). To compare the simulation predictions with our experimental results, we calculate the normalized concentration as the number density of DNA molecules for each data point normalized by the bulk number density.

Figure 8 predicts that the depletion-layer thickness (defined again as the position at which the concentration is half that of the bulk) at $Wi = 10$ is about 10 μm, which is roughly twice as thick as found in our experimental data and is therefore in much closer agreement with the experiments than is the dumbbell theory.[21] However, the BD simulations predict that it takes at least 8 h (~8000 relaxation times of DNA) for the concentration

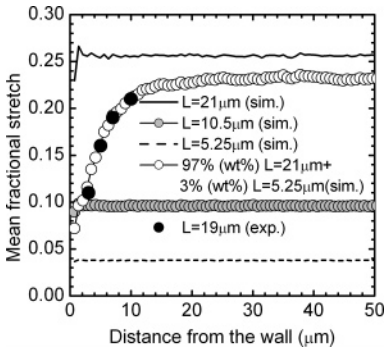

Figure 9. Comparison of steady-state mean fractional stretch in BD simulations of DNA molecules of various lengths and with a mixture of lengths in shear flow above a surface at $Wi = 10$ with the experimental results of dilute solutions of nominally intact DNA at $Wi = 10.3$. In the simulations, the stretch lengths of all DNA molecules, including the short ones, are normalized by $L = 21$ μm.

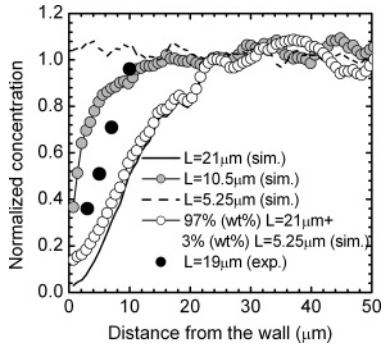

Figure 10. Same as in Figure 9, except for normalized concentration, rather than mean fractional stretch.

of λ-DNA molecules to reach the steady state, which is still an order of magnitude longer than measured in the experiments. Similar, but smaller discrepancies in the thickness of the depletion layer and the time to reach the steady state between experiments and BD simulations have also been reported by Chen et al.[5] for T2 DNA in a microchannel with an oscillatory pressure-driven flow.

The simulations also predict in Figure 9 that the steady-state mean fractional stretch of the molecules with the same length does not change at different distances above the bottom surface, but that shorter chains have a smaller mean stretch due to the decrease of the real *Wi*. Figure 10 indicates that with an increase of DNA length, the thickness of the depletion layer increases at steady state. By assuming 3% (wt%) of the 21 μm-long DNA molecules are broken, each into four 5.25 μm-long fragments, the simulation is able to match the experimental mean fractional stretch (shown in Figure 9); however, with 3% fragments, the predicted depletion layer thickness is still greater than in the steady-state experimental results (shown in Figure 10).

The simulation results imply that the decrease of the stretch with time observed in the experiments is caused by the presence of shorter chains in nominally "intact" λ-phage DNA solutions, and that a small percentage of the chains is probably broken. We note that in other experiments with solutions of λ-phage DNA molecules reported in the literature, the presence of a small percentage of broken chains would likely have been completely undetected. The DNA migration effect near a wall is exquisitely sensitive to such short chains, as full-length chains are almost entirely pushed away from the wall, and the length of the remaining chains is revealed by their stretch. Nevertheless, even allowing for the presence of shorter chains in the simulations, we are still unable to explain quantitatively the observed time dependence of the DNA concentration profile, which suggests that some aspects of polymer migration near surfaces is missing in models developed thus far. In the accompanying paper, the effect of the finite DNA concentration is considered, where it is confirmed that the concentration of DNA used here is too low for finite concentration effects to influence migration. Since we saw that at high *Wi* the dumbbell model greatly over-predicts (by a factor of 10) the width of the wall depletion layer at $Wi = 10$, while simulations of chains with 10 springs reduce the discrepancy to a factor of 2, it is possible that if we could carry out simulations of chains with dozens of springs, with full wall-influenced HI, that the wall depletion thickness might gradually diminish and finally come close to the experimental value. In bulk flow, high-*Wi* shear-flow simulations with 10 springs predict somewhat more stretching (around 10% more on average) than is obtained with highly refined bead−rod models and in experiments.[39] While this discrepancy is quite modest for bulk shear, possibly the difference is larger for the wall migration effect. At any rate, it seems clear that shear-induced polymer migration and chain stretch are extremely sensitive not only to physical parameters such as shear rate and a slight polydispersity in polymer chain length but also to how well the polymer is modeled. Hence, further efforts to predict wall hydrodynamic effects quantitatively may lead to more accurate polymer modeling.

Conclusions

Optical imaging of λ-phage DNA molecules was used to measure the time-dependent polymer concentration and stretch near a non-adsorbing solid surface in a torsional shear flow. We found, as observed in other geometries, that polymer chains migrate away from the surface in dilute solutions. The migration is enhanced near surfaces with a larger depletion layer created at higher *Wi*, in qualitative, but not quantitative, agreement with the predictions of the FENE-P dumbbell model.[21] The experimental depletion layer at $Wi = 10$ is an order of magnitude thinner than expected from those predictions, which results in a shorter time (by more than an order of magnitude) for the concentration to reach steady state in the experiments. The time scale for migration in the experiments is roughly the time for molecules to diffuse over the depletion layer, which is consistent with the theory, given the thinner experimental depletion layer. With an increase of *Wi* from 5.0 to 20.4, this time scale increases from around 40 min to around 100 min, as expected qualitatively from the theory. Simulations with 10-spring chains are in closer agreement with the experiments than are the dumbbell predictions, but the simulated depletion layer remains twice as thick as the experimental one, and the simulated migration time is still an order of magnitude larger than observed. The discrepancies indicate that further study of migration effects of polymers under shear near surfaces is warranted, including more simulations with more refined polymer models.

Over the time scale of migration, the experimental mean fractional stretch decreases with time near the surface after the startup of steady shear. Addition of DNA fragments leads to a net decrease in the migration rate, and a decrease in the stretch near the surface. This suggests that the presence of a small percentage of fragmented DNA might be responsible for the observed low stretch near the surface.

Acknowledgment. We are grateful for financial support from the NASA microgravity research division (Grant NAG3-2708) and from the National Science Foundation (Grant NSF-NSEC EEC-0425626).

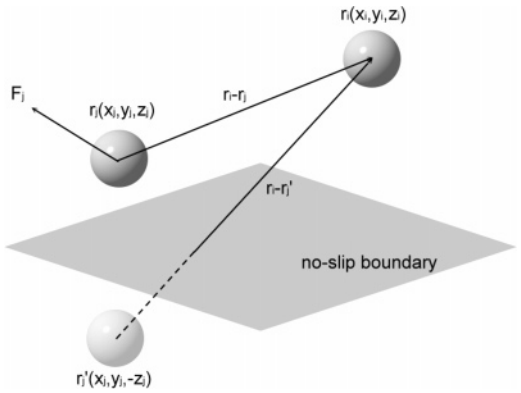

Figure 11. Illustration of the vector system. For the modified RPY tensor and the Blake−Oseen−Burgers tensor, the spheres reduce to points.

Appendix: Modified Rotne-Prager-Yamakawa Tensor

To describe the HI between two spheres, the simplest approach is to assume that the spheres have negligible volume and thus can be considered as two points (i.e., their radius is small compared to their separation). In this way, the perturbed flow $\mathbf{v}'$ induced by a force $\mathbf{F}_j$ acting on sphere j at $\mathbf{r}_j(x_j, y_j, z_j)$ (see Figure 11) has an effect on another sphere i at $\mathbf{r}_i(x_i, y_i, z_i)$ that can be obtained by solving the Stokes equation along with the equation of continuity:

$$0 = -\nabla p + \eta_s \nabla^2 \mathbf{v}' + \mathbf{F}_j \delta(\mathbf{r}_i - \mathbf{r}_j) \tag{A1}$$

$$\nabla \cdot \mathbf{v}' = 0 \tag{A2}$$

where p is the pressure, η_s is the fluid viscosity, and δ is the Dirac delta function. The solution to eqs A1 and A2, including the effect of the boundary conditions, can be expressed in a general form as

$$\mathbf{v}' = \mathbf{\Omega}_{ij} \cdot \mathbf{F}_j \tag{A3}$$

where $\mathbf{\Omega}_{ij}$ is the HI tensor which will be defined in detail later. From the HI tensor, we can construct the diffusion tensor $\mathbf{D}_{ij}$ for use in BD simulations:

$$\mathbf{D}_{ij} = k_B T \left[\frac{1}{6\pi\eta_s a} \mathbf{I}\delta_{ij} + \mathbf{\Omega}_{ij} \right] \tag{A4}$$

where a is the hydrodynamic radius of the spheres.

The best known HI tensor is the Oseen−Burgers (OB) tensor $\mathbf{\Omega}^{OB}(\mathbf{r}_i,\mathbf{r}_j)$ obtained by solving eqs A1 and A2 with the no-slip boundary condition applied on the surface infinitely far from r_j. Therefore, the OB tensor represents the HI in the bulk flow where the wall effect is absent. The OB tensor can be written as

$$\mathbf{\Omega}_{ij}^{OB} = \mathbf{\Omega}^{OB}(\mathbf{r}_i,\mathbf{r}_j) = \frac{1}{8\pi\eta_s|\mathbf{r}_i - \mathbf{r}_j|}\left[\mathbf{I} + \frac{(\mathbf{r}_i - \mathbf{r}_j)(\mathbf{r}_i - \mathbf{r}_j)}{|\mathbf{r}_i - \mathbf{r}_j|^2}\right] \tag{A5}$$

where $\mathbf{I}$ is the unit tensor. And $\mathbf{\Omega}_{ij}$ in eq A4 is defined by

$$\mathbf{\Omega}_{ij} = (1 - \delta_{ij})\mathbf{\Omega}_{ij}^{OB} \tag{A6}$$

For the OB tensor, $\mathbf{D}_{ij}$ equals $\mathbf{D}_{ji}$, implying that the HI is only a function of the relative position between spheres, not their absolute positions. However, if a boundary is nearby, the above symmetry is broken and a new HI tensor is needed to include the wall effect.

Blake[42] derived the velocity and the pressure fields for Stokes' flow due to a point force in the vicinity of a stationary plane boundary by solving eqs A1 and A2 with the boundary condition $\mathbf{v}'(x_i, y_i, z_i = 0) = 0$. The Blake−Oseen−Burgers (BOB) tensor can be expressed as

$$\mathbf{\Omega}_{ij}^{BOB} = \mathbf{\Omega}^{OB}(\mathbf{r}_i,\mathbf{r}_j) - \mathbf{\Omega}^{OB}(\mathbf{r}_i,\mathbf{r}_j') + \Delta\mathbf{\Omega}^{OB}(\mathbf{r}_i,\mathbf{r}_j')$$
$$\mathbf{r}_i = (x_i,y_i,z_i),\ \mathbf{r}_j = (x_j,y_j,z_j),\ \mathbf{r}_j' = (x_j,y_j,-z_j) \tag{A7}$$

where $\mathbf{r}_j'$ is the image of $\mathbf{r}_j$ relative to the wall (see Figure 11), $\Delta\mathbf{\Omega}^{OB}(\mathbf{r}_i,\mathbf{r}_j')$ is defined by Blake,[41] which is the first term of $\Delta\mathbf{\Omega}^{RPY}(\mathbf{r}_i,\mathbf{r}_j')$, given below in eq A17. Thus, $\mathbf{\Omega}_{ij}$ in eq A4 in this case is given by

$$\mathbf{\Omega}_{ij} = (1 - \delta_{ij})\mathbf{\Omega}^{OB}(\mathbf{r}_i,\mathbf{r}_j) - \mathbf{\Omega}^{OB}(\mathbf{r}_i,\mathbf{r}_j') + \Delta\mathbf{\Omega}^{OB}(\mathbf{r}_i,\mathbf{r}_j') \tag{A8}$$

Equation A8 is different from eq A6 because the presence of the wall affects the self-diffusivity of sphere j.

Although the BOB tensor includes the wall effect, like the OB tensor it fails to account for the finite volume of the spheres, and thus is only accurate when the separation between two spheres is large relative to their diameters. Moreover, both tensors become non-positive-definite when the separation between centers of the spheres is smaller than the diameter of the spheres. The above problems are overcome by the Rotne−Prager (RP) tensor, which includes the effect of the finite volume of the spheres and furthermore separates the calculation of the hydrodynamic tensor into two parts, one for the separation between the centers of spheres larger than twice the radius of the spheres, the other for separations smaller than twice the sphere radius. Yamakawa,[32] on the other hand, used the Taylor expansion to derive a first order correction to the OB tensor for the HI between two spheres. Since the tensor given by Yamakawa is identical to the RP tensor for non-overlapping spheres ($R_{ij} > 2a$), the RP tensor is often called the RPY tensor.

$$\mathbf{\Omega}_{ij}^{RPY} = \mathbf{\Omega}^{RPY}(\mathbf{r}_i,\mathbf{r}_j) =$$
$$\frac{1}{8\pi\eta_s|\mathbf{r}_i - \mathbf{r}_j|}\left[C_1\mathbf{I} + C_2\frac{(\mathbf{r}_i - \mathbf{r}_j)(\mathbf{r}_i - \mathbf{r}_j)}{|\mathbf{r}_i - \mathbf{r}_j|^2}\right], \quad if\ |\mathbf{r}_i - \mathbf{r}_j| \geq 2a$$
$$= \frac{1}{6\pi\eta_s|\mathbf{r}_i - \mathbf{r}_j|}\left[C_3\mathbf{I} + C_4\frac{(\mathbf{r}_i - \mathbf{r}_j)(\mathbf{r}_i - \mathbf{r}_j)}{|\mathbf{r}_i - \mathbf{r}_j|^2}\right], \quad if\ |\mathbf{r}_i - \mathbf{r}_j| < 2a \tag{A9}$$

where

$$C_1 = 1 + \frac{2a^2}{3|\mathbf{r}_i - \mathbf{r}_j|^2}, \quad C_2 = 1 - \frac{2a^2}{|\mathbf{r}_i - \mathbf{r}_j|^2}$$
$$C_3 = 1 - \frac{9|\mathbf{r}_i - \mathbf{r}_j|}{32a}, \quad C_4 = \frac{3|\mathbf{r}_i - \mathbf{r}_j|}{32a}$$

Because of the lack of a wall effect, $\mathbf{\Omega}_{ij}$ is defined the same as in eq A6

$$\mathbf{\Omega}_{ij} = (1 - \delta_{ij})\mathbf{\Omega}_{ij}^{RPY} \tag{A10}$$

In the following discussion, by "RPY tensor" we mean the HI tensor for non-overlapping spheres.

To include wall effect into the HI tensor, Bossis et al.[33] combined multipole expansions of the velocity field and Faxen's

equations to relate the fluid velocity to the bead velocity. The very general HI tensor given by Bossis et al.[33] includes the lubrication force and higher order terms that become important when the bead-wall separation is comparable to the bead−bead separation. However, one can also modify the BOB tensor to include the finite volume effect and obtain the same expression of Bossis et al.[33] except for the lubrication force. Yamakawa first demonstrated that the velocity perturbation around a sphere can be represented by the velocity perturbation induced by point forces equal to the frictional force of the sphere uniformly distributed on the surface of the sphere. In other words, if a sphere of radius σ_j at $\mathbf{r}_j$ exerts a force $\mathbf{F}_j$ on the fluid, the induced velocity perturbation $\mathbf{v}'$ at $\mathbf{r}_i$ can be approximated by

$$\mathbf{v}' = \langle \mathbf{\Omega}^{OB}(\mathbf{r}_i,\mathbf{r}_j + \boldsymbol{\sigma}_j)\rangle \cdot \mathbf{F}_j \tag{A11}$$

where $\langle\ \rangle$ indicates average over all possible orientations of radius vector $\boldsymbol{\sigma}_j$. Equation A11 can be expanded in a Taylor series. Using $\langle \boldsymbol{\sigma}_j \rangle = 0$ and $\langle \boldsymbol{\sigma}_j \boldsymbol{\sigma}_j \rangle = {}^1/_3 \sigma_j^2 \mathbf{I}$, and discarding higher order terms, one obtains

$$\mathbf{v}' = \left[\mathbf{\Omega}^{OB}(\mathbf{r}_i,\mathbf{r}_j) + \frac{\sigma_j^{\,2}}{6}\nabla_j^{\,2}\mathbf{\Omega}^{OB}(\mathbf{r}_i,\mathbf{r}_j)\right]\cdot\mathbf{F}_j \tag{A12}$$

Equation A12 describes the perturbed flow by a force $\mathbf{F}_j$ acting on a sphere with its center at $\mathbf{r}_j$. Using the same method, one can obtain the perturbed flow acting on a sphere with its center at $\mathbf{r}_i$ by a force $\mathbf{F}_j$ acting on another sphere with its center at $\mathbf{r}_j$:

$$\mathbf{v}' = \langle \mathbf{\Omega}^{OB}(\mathbf{r}_i + \sigma_i,\mathbf{r}_j + \sigma_j)\rangle \cdot \mathbf{F}_j = \mathbf{\Omega}^{RPY}(\mathbf{r}_i,\mathbf{r}_j)\cdot\mathbf{F}_j \tag{A13}$$

where σ_i and σ_j are the radii of sphere i and j, respectively, the radii vectors are $\boldsymbol{\sigma}_j$ and $\boldsymbol{\sigma}_i$, and here the average is over all orientations of both vectors.

To derive the modified Rotne−Prager−Yamakawa (MRPY) tensor for non-overlapping spheres in the vicinity of a wall, in eq A13, we replace $\mathbf{\Omega}^{OB}(\mathbf{r}_i,\mathbf{r}_j)$ with $\mathbf{\Omega}^{BOB}(\mathbf{r}_i,\mathbf{r}_j)$, given by eq A7:

$$\mathbf{v}' = \langle \mathbf{\Omega}^{BOB}(\mathbf{r}_i + \sigma_i,\mathbf{r}_j + \sigma_j)\rangle \cdot \mathbf{F}_j = \mathbf{\Omega}^{MRPY}(\mathbf{r}_i,\mathbf{r}_j)\cdot\mathbf{F}_j \tag{A14}$$

Therefore, the MRPY tensor can be expressed as

$$\begin{aligned}\mathbf{\Omega}^{MRPY}(\mathbf{r}_i,\mathbf{r}_j) &= \langle \mathbf{\Omega}^{BOB}(\mathbf{r}_i + \boldsymbol{\sigma}_i,\mathbf{r}_j + \boldsymbol{\sigma}_j)\rangle \\ &= \mathbf{\Omega}^{BOB}(\mathbf{r}_i,\mathbf{r}_j) + \frac{\sigma_i^{\,2}}{6}\nabla_i^{\,2}\mathbf{\Omega}^{BOB}(\mathbf{r}_i,\mathbf{r}_j) + \frac{\sigma_j^{\,2}}{6}\nabla_j^{\,2}\mathbf{\Omega}^{BOB}(\mathbf{r}_i,\mathbf{r}_j) + \ldots \\ &= \mathbf{\Omega}^{RPY}(\mathbf{r}_i,\mathbf{r}_j) - \mathbf{\Omega}^{RPY}(\mathbf{r}_i,\mathbf{r}_j') + \Delta\mathbf{\Omega}^{RPY}(\mathbf{r}_i,\mathbf{r}_j')\end{aligned} \tag{A15}$$

Thus,

$$\mathbf{\Omega}_{ij} = (1-\delta_{ij})\mathbf{\Omega}^{RPY}(\mathbf{r}_i,\mathbf{r}_j) - \mathbf{\Omega}^{RPY}(\mathbf{r}_i,\mathbf{r}_j') + \Delta\mathbf{\Omega}^{RPY}(\mathbf{r}_i,\mathbf{r}_j') \tag{A16}$$

By taking $\sigma_i = \sigma_j = a$ into the MRPY tensor, we obtain the detailed expression for $\Delta\mathbf{\Omega}^{RPY}(\mathbf{r}_i,\mathbf{r}_j')$ as follows,

$$8\pi\eta_s\,\Delta\mathbf{\Omega}_{xx}^{RPY} = -2z_iz_j\left[\frac{1}{R^3} - 3\frac{(x_i-x_j)^2}{R^5}\right] + 2a^2(z_i+z_j)^2\left[\frac{1}{R^5} - \frac{5(x_i-x_j)^2}{R^7}\right]$$

$$8\pi\eta_s\,\Delta\mathbf{\Omega}_{yy}^{RPY} = -2z_iz_j\left[\frac{1}{R^3} - 3\frac{(y_i-y_j)^2}{R^5}\right] + 2a^2(z_i+z_j)^2\left[\frac{1}{R^5} - \frac{5(y_i-y_j)^2}{R^7}\right]$$

$$8\pi\eta_s\,\Delta\mathbf{\Omega}_{zz}^{RPY} = 2z_iz_j\left[\frac{1}{R^3} - 3\frac{(z_i+z_j)^2}{R^5}\right] + 2a^2(z_i+z_j)^2\left[\frac{-3}{R^5} + \frac{5(z_i+z_j)^2}{R^7}\right]$$

$$8\pi\eta_s\,\Delta\mathbf{\Omega}_{xy}^{RPY} = 8\pi\eta_s\,\Delta\mathbf{\Omega}_{yx}^{RPY} = 6\frac{z_iz_j(x_i-x_j)(y_i-y_j)}{R^5} - \frac{10a^2(z_i+z_j)^2(x_i-x_j)(y_i-y_j)}{R^7}$$

$$8\pi\eta_s\,\Delta\mathbf{\Omega}_{xz}^{RPY} = 2(x_i-x_j)\left[\frac{z_j}{R^3} - 3\frac{z_iz_j(z_i+z_j)}{R^5}\right] - 2a^2(x_i-x_j)\left[\frac{2(z_i+z_j)}{R^5} - \frac{5(z_i+z_j)^3}{R^7}\right]$$

$$8\pi\eta_s\,\Delta\mathbf{\Omega}_{zx}^{RPY} = 2(x_i-x_j)\left[\frac{z_j}{R^3} + 3\frac{z_iz_j(z_i+z_j)}{R^5}\right] - 2a^2(x_i-x_j)\left[\frac{5(z_i+z_j)^3}{R^7}\right]$$

$$8\pi\eta_s\,\Delta\mathbf{\Omega}_{yz}^{RPY} = 2(y_i-y_j)\left[\frac{z_j}{R^3} - 3\frac{z_iz_j(z_i+z_j)}{R^5}\right] - 2a^2(y_i-y_j)\left[\frac{2(z_i+z_j)}{R^5} - \frac{5(z_i+z_j)^3}{R^7}\right]$$

$$8\pi\eta_s\,\Delta\mathbf{\Omega}_{zy}^{RPY} = 2(y_i-y_j)\left[\frac{z_j}{R^3} + 3\frac{z_iz_j(z_i+z_j)}{R^5}\right] - 2a^2(y_i-y_j)\left[\frac{5(z_i+z_j)^3}{R^7}\right] \tag{A17}$$

where $R = |\mathbf{r}_i - \mathbf{r}_i|$

We notice that if $\sigma_i \neq \sigma_j$ one can obtain the HI between spheres of two different sizes. This newly derived MRPY tensor obeys the reciprocity relation:

$$\mathbf{\Omega}(\mathbf{r}_i,\mathbf{r}_j) = \mathbf{\Omega}^T(\mathbf{r}_j,\mathbf{r}_i) \tag{A18}$$

which follows from the self-adjointness of the Stokes operator. In some studies, the reciprocity relation was violated,[18,19,43] and the average of $\mathbf{\Omega}(\mathbf{r}_i,\mathbf{r}_j)$ and $\mathbf{\Omega}^T(\mathbf{r}_j,\mathbf{r}_i)$ was used to replace $\mathbf{\Omega}(\mathbf{r}_i,\mathbf{r}_j)$ and $\mathbf{\Omega}^T(\mathbf{r}_j,\mathbf{r}_i)$ to enforce the reciprocity relation. The MRPY tensor reduces to the BOB tensor as the sphere radius approaches zero, and reduces to the RPY tensor if the spheres are far from the wall.

References and Notes

(1) Ausserré, D.; Hervet, H.; Rondelez, F. *Macromolecules* **1986**, *19*, 85−88.
(2) Ausserré, D.; Edwards, J.; Lecourtier, J.; Hervet, H.; Rondelez, F. *Europhys. Lett.* **1991**, *14*, 33−38.
(3) Rondelez, F.; Ausserre, D.; Hervet, H. *Annu. Rev. Physiol. Chem.* **1987**, *38*, 317−347.
(4) Fang, L.; Hu, H.; Larson, R. G. *J. Rheol.* **2005**, *49*, 127−138.

(5) Chen, Y. L.; Graham, M. D.; de Pablo, J. J.; Jo, K.; Schwartz, D. C. *Macromolecules* **2005**, *38*, 6680−6687.
(6) Agarwal, U. S.; Dutta, A.; Mashelkar, R. A. *Chem. Eng. Sci.* **1994**, *49*, 1693−1717.
(7) Garner, F. H.; Nissan, A. H. *Nature (London)* **1946**, *158*, 634−635.
(8) Aubert, J. H.; Prager, S.; Tirrell, M. *J. Chem. Phys.* **1980**, *73*, 4103−4112.
(9) Aubert, J. H.; Tirrell, M. *J. Chem. Phys.* **1980**, *72*, 2694−2701.
(10) Bhave, A. V.; Armstrong, R. C.; Brown, R. A. *J. Chem. Phys.* **1991**, *95*, 2988−3000.
(11) Larson, R. G. *Rheol. Acta* **1992**, *31*, 497−520.
(12) Mavrantzas, V. G.; Beris, A. N. *J. Rheol.* **1992**, *36*, 175−213.
(13) Mavrantzas, V. G.; Beris, A. N. *J. Chem. Phys.* **1999**, *110*, 616−627.
(14) Mavrantzas, V. G.; Beris, A. N. *J. Chem. Phys.* **1999**, *110*, 628−638.
(15) Woo, N. J.; Shaqfeh, E. S. G.; Khomami, B. *J. Rheol.* **2004**, *48*, 281−298.
(16) Woo, N. J.; Shaqfeh, E. S. G.; Khomami, B. *J. Rheol.* **2004**, *48*, 299−318.
(17) Chopra, M.; Larson, R. G. *J. Rheol.* **2002**, *46*, 831−862.
(18) Jendrejack, R. M.; Dimalanta, E. T.; Schwartz, D. C.; Graham, MLarson. D.; de Pablo, J. J. *Phys. Rev. Lett.* **2003**, *91*, 038102.
(19) Jendrejack, R. M.; Schwartz, D. C.; de Pablo, J. J.; Graham, M. D. *J. Chem. Phys.* **2004**, *120*, 2513−2529.
(20) Li, L.; Hu, H.; Larson, R. G. *Rheol. Acta* **2004**, *44*, 38−46.
(21) Ma, H. B.; Graham, M. D. *Phys. Fluids* **2005**, *17*, 083103.
(22) Hu, H.; Larson, R. G.; Magda, J. J. *J. Rheol.* **2002**, *46*, 1001−1021.
(23) Bustamante, C.; Marko, J. F.; Siggia, E. D.; Smith, S. *Science* **1994**, *265*, 1599−1600.
(24) Smith, D. E.; Chu, S. *Science* **1998**, *281*, 1335−1340.
(25) Perkins, T. T.; Smith, D. E.; Chu, S. *Science* **1997**, *276*, 2016−2021.
(26) Smith, D. E.; Babcock, H. P.; Chu, S. *Science* **1999**, *283*, 1724−1727.
(27) Chapman, R. E.; Klotz, L. C.; Thompson, D. S.; Zimm, B. H. *Macromolecules* **1969**, *2*, 637−643.
(28) Chen, Y. L.; Graham, M. D.; de Pablo, J. J.; Randall, G. C.; Gupta, M.; Doyle, P. S. *Phys. Rev. E* **2004**, *70*, 060901.
(29) Saintillan, D.; Shaqfeh, E. S. G.; Darve, E. *J. Fluid Mech.* **2006**, *557*, 297−306.
(30) Hsieh, C. C.; Li, L.; Larson, R. G. *J Non-Newton Fluid* **2003**, *113*, 147−191.
(31) Rotne, J.; Prager, S. *J. Chem. Phys.* **1969**, *50*, 4831−4837.
(32) Yamakawa, H. *J. Chem. Phys.* **1970**, *53*, 436−440.
(33) Bossis, G.; Meunier, A.; Sherwood, J. D. *Phys. Fluids A: Fluid* **1991**, *3*, 1853−1858.
(34) Jendrejack, R. M.; de Pablo, J. J.; Graham, M. D. *J. Chem. Phys.* **2002**, *116*, 7752−7759.
(35) Harnau, L.; Winkler, R. G.; Reineker, P. *J. Chem. Phys.* **1996**, *104*, 6355−6368.
(36) Smith, D. E.; Perkins, T. T.; Chu, S. *Macromolecules* **1996**, *29*, 1372−1373.
(37) Larson, R. G. *Constitutive Equations for Polymer Melts and Solutions*, Butterworths: Boston, MA, 1988.
(38) Dill, K. A.; Zimm, B. H. *Nucleic Acids Res.* **1979**, *7*, 735−749.
(39) Hur, J. S.; Shaqfeh, E. S. G.; Babcock, H. P.; Smith, D. E.; Chu, S. *J. Rheol.* **2001**, *45*, 421−450.
(40) Liu, Y. Y.; Wang, P. Y.; Dou, S. X.; Wang, W. C.; Xie, P.; Yin, H. W.; Zhang, X. D. *J. Chem. Phys.* **2004**, *121*, 4302−4309.
(41) Larson, R. G. *J. Rheol.* **2005**, *49*, 1−70.
(42) Blake, J. R. *Proc. Camb. Philos. S-M* **1971**, *70*, 303−310.
(43) Jendrejack, R. M.; Schwartz, D. C.; Graham, M. D.; de Pablo, J. J. *J. Chem. Phys.* **2003**, *119*, 1165−1173.

MA062630C